View metadata, citation and similar papers at core.ac.uk

brought to you by CORE

provided by IntechOpen

We are IntechOpen, the world's leading publisher of Open Access books Built by scientists, for scientists

4,800
Open access books available

122,000
International authors and editors

135M
Downloads

Our authors are among the

154
Countries delivered to

TOP 1%
most cited scientists

12.2%
Contributors from top 500 universities

WEB OF SCIENCE™

Selection of our books indexed in the Book Citation Index in Web of Science™ Core Collection (BKCI)

Interested in publishing with us?
Contact book.department@intechopen.com

Numbers displayed above are based on latest data collected.
For more information visit www.intechopen.com

Chapter 6

Effect of Microstructure Transformations on Fatigue Properties of Laser Beam Welded Ti-6Al-4V Butt Joints Subjected to Postweld Heat Treatment

Fedor Fomin, Volker Ventzke, Falk Dorn,
Nikita Levichev and Nikolai Kashaev

Additional information is available at the end of the chapter

http://dx.doi.org/10.5772/66178

Abstract

The effect of postweld heat treatment (PWHT) on 2.6-mm-thick Ti-6Al-4V butt joints that were welded using a continuous-wave 8-kW ytterbium fibre laser was studied in terms of the microstructure, microtexture, number of welding defects, microhardness, residual stress distribution and high cycle fatigue (HCF) properties. Five types of heat treatments in the temperature range of 540–920°C are investigated. The main reasons leading to fatigue life deterioration after the laser welding process are discussed, and possible guidelines for further improvement of the HCF behaviour by a subsequent suitable type of PWHT are provided. Low-temperature annealing ($T < 600$°C) tends to harden both the base material and the welding zone without any significant effect on the fatigue properties. Heat treatments at higher temperatures ($T > 750$°C) lead to the transformation of a strong martensitic structure in the fusion zone (FZ) into more ductile coarse lamellar, which is more beneficial for fatigue performance. A suitable type of PWHT can increase the fatigue limit of a laser-welded Ti-6Al-4V butt joint by 10%; however, a slight decrease in static strength should be considered. The effect of stress relief at elevated temperatures is studied.

Keywords: titanium alloy, Ti-6Al-4V, laser beam welding, heat treatment, microstructure, fatigue, residual stress

1. Introduction

Designed in the 1950s and initially used for compressor blades in gas turbine engines, Ti-6Al-4V titanium alloy has a high specific strength, stability at temperatures up to 400°C and good

INTECH
open science | open minds

© 2016 The Author(s). Licensee InTech. This chapter is distributed under the terms of the Creative Commons Attribution License (http://creativecommons.org/licenses/by/3.0), which permits unrestricted use, distribution, and reproduction in any medium, provided the original work is properly cited. CC BY

corrosion resistance. These properties have brought about an extensive use of Ti-6Al-4V in a variety of applications, such as aerospace, biomedical devices and chemical processing equipment. The aircraft industry accounts for more than 80% of this usage [1]. Airframes and aeroengine parts are the two most common applications for titanium alloys. The relatively high costs of both the raw material and the part fabrication continue to hinder the wider use of titanium in applications where weight and corrosion are not critical factors. In this context, more efficient technologies for producing complex titanium structures are required to broaden the application areas of titanium alloys and minimize the inherent cost problem. Laser beam welding (LBW) is a very promising joining technique that provides the possibility of high productivity, a single-step process and the benefit of potential weight savings compared with riveting. Compared with most structural titanium alloys, Ti-6Al-4V is considered to be highly weldable. The high energy density of the laser beam enables relatively high welding speed, which results in low heat input, a narrow heat-affected zone (HAZ) and low distortion. LBW has become increasingly competitive as a joining process over the last few decades owing to significant practical advantages over electron beam welding (EBW), requiring a high vacuum environment. However, additional measures must be taken to protect the weld zone from atmospheric contamination during LBW.

A number of researchers have investigated the influence of welding parameters on the quality and mechanical properties of the laser beam welded Ti-6Al-4V butt joints [2–5]. Generally, fusion zones exhibit higher strength and lower ductility than those of the base metal, and fracture of transverse-oriented butt welds in tensile testing usually occurs in the unaffected parent material [2, 5]. Despite the generally higher tensile strength, inferior fatigue properties of laser beam welded titanium joints are commonly observed. Because Ti-6Al-4V alloy is primarily used in fatigue-critical components, poor axial fatigue behaviour of laser beam welded Ti-6Al-4V joints is one of the main factors limiting their wide industrial application. In consideration of the above-mentioned problems, more complete understanding of the reasons and mechanisms for fatigue failure of laser beam welded Ti-6Al-4V joints is of great scientific interest.

Because the control of microstructure is the primary key for obtaining required mechanical properties in titanium alloys, postweld heat treatment (PWHT), which results in the transformation of the welding zone microstructure, is one of the options aiming to achieve improved fatigue performance of laser beam welded Ti-6Al-4V butt joints. Kabir et al. [6] investigated the effects of stress relief annealing and solution heat treatment followed by ageing on the microstructure, hardness and tensile properties of autogenously welded Ti-6Al-4V butt joints. Increased microhardness in the fusion zone after stress relief annealing was observed. The joint efficiency in terms of tensile strength was maximum for the as-welded condition and was slightly decreased by nearly 5% for solution heat-treated and aged conditions. Babu et al. [7] studied the influence of two types of heat treatment (700 and 900°C) on the fatigue properties of electron beam welded Ti-6Al-4V butt joints. The specimens annealed at lower temperatures exhibited longer fatigue lives and higher tensile strength. These results were attributed to the coarsening of the microstructure in the fusion zone after PWHT at high temperatures. Tsai et al. [8] showed that heat treatment at a temperature of 790°C for 1 h followed by air cooling can

http://dx.doi.org/10.5772/66178

noticeably improve mechanical properties and provide the electron beam welded joint with a superior combination of tensile strength and ductility. Friction stir welded Ti-6Al-4V joints subjected to various types of heat treatments were studied by Edwards et al. [9], who found that hardness and strength decreased with increasing heat treatment temperature, but ductility and fatigue performance improved. It was recommended that a high heat treatment temperature can be used to obtain the best combination of strength, ductility and fatigue performance. Thus, extensive research work has been carried out on welding of Ti-6Al-4V alloy and the subsequent PWHT. However, most of the published information is focusing on the static tensile properties. There is a lack of clarity about the influence of PWHT on the high cycle fatigue (HCF) behavior of the LBW Ti-6Al-4v butt joints. The present study was undertaken to quantitatively characterize the effect of heat treatment on the HCF performance of the laser beam welded Ti-6Al-4V butt joints and link this effect with microstructural transformations that took place during PWHT.

2. Experimental

2.1. Material

The material used in this study was Ti-6Al-4V (Grade 5, AMS 4911) alloy in the form of hot-rolled and mill-annealed sheets with a thickness of 2.6 mm supplied by VSMPO-AVISMA Corporation, Russia. The chemical composition of the base material (BM) determined by energy dispersive X-ray (EDX) spectroscopy is given in **Table 1**. The mechanical properties of the material in the final rolling direction are listed in **Table 2**. Coupons of size 190 mm × 110 mm × 2.6 mm were extracted from the as-received sheet for welding experiments. The dimensions of the coupons were sufficiently long to extract seven fatigue specimens from each after welding.

	Al	V	Fe	Si	Ti
Ti-6Al-4V	6.54	3.31	0.16	0.35	89.64

Table 1. Chemical composition (wt.%) of the Ti-6Al-4V alloy in original as-received condition determined by EDX analysis.

Modulus of elasticity, E	110.9 ± 0.5 GPa
Yield strength, $R_{p0.2}$	995.3 ± 9.5 MPa
Ultimate tensile strength, R_m	1039.2 ± 11.4 MPa
Elongation at break, A	19.2 ± 0.6%

Note: Average values with standard deviation of three tested specimens.

Table 2. Mechanical properties of the Ti-6Al-4V alloy in the final rolling direction.

2.2. Laser beam welding

The welding equipment consisted of an 8-kW continuous-wave ytterbium fibre laser YLS-8000-S2-Y12 (IPG Photonics Corporation) integrated with an IXION ULM 804 CNC-controlled universal laser machine. A collimation lens of 120 mm, a focal length of 300 mm and a process fibre with a diameter of 600 μm were employed to produce a focal spot diameter of approximately 700 μm. The centre wavelength of the fibre laser was 1070 nm. The divergence half-angle of the focused multimode beam was 30.3 mrad, and the resulting beam parameter product BPP = 11.3 mm*mrad.

Prior to welding, the faying edges of the specimens were machined, ground and then thoroughly cleaned with ethanol to remove any surface oxides and contaminants. Preliminary welding experiments with small coupons were conducted to identify the optimal combination of welding parameters and obtain a good weld quality and an appropriate weld shape. The parameters finally chosen and employed for welding of coupons are listed in **Table 3**. The specimens were fixed in an open plastic box filled with Ar to protect the weld bead from air during the LBW process. The uniform Ar flow around the weld bead was provided by the injection of the shielding gas through the porous Al plate at the bottom of the box. Kashaev et al. reported based on hot gas extraction analysis that this shielding technique was very effective [5]. The welding direction was perpendicular to the rolling direction of the material.

Laser power	5500 W
Welding speed	4.0 m/min
Focal position	-3.0 mm
Filler wire	Ti Grade 5, Ø 1.0 mm
Filler wire feed rate	3.0 m/min
Shielding	Argon, 15 l/min

Table 3. Laser beam welding process parameters.

2.3. Postweld heat treatment

Postweld heat treatment was conducted using Workhorse vacuum furnace, Centorr Vacuum Industries, USA, at a vacuum degree of 0.1 Pa. The parameters of different types of PWHT are given in **Table 4**. Annealing temperatures did not exceed the β transus, which is nearly 995°C for the Ti-6Al-4V alloy [1, 2]. During heat treatment, the welded plates were hung using molybdenum wire to prevent any contact between the specimens and furnace wall. No significant distortion was observed after heat treatment. Cooling to room temperature was performed in Ar atmosphere. All heat-treated specimens were then machined from both sides before extracting the fatigue specimens.

http://dx.doi.org/10.5772/66178

Stress relief annealing, SRA1	540°C/4 h/AC
Stress relief annealing, SRA2	650°C/2 h/AC
Full annealing, FA1	750°C/2 h/AC
Full annealing, FA2	850°C/1 h/AC
Recrystallization annealing, RA	920°C/45 min/AC
Duplex annealing, DA	RA + SRA1

Table 4. Conditions of postweld heat treatment.

2.4. Microstructural characterization

Transverse cross sections were cut from the stable middle region of the joint for metallographic examination and microhardness testing. After sectioning, the samples were mounted, ground and polished using an oxide polishing suspension (OPS) compound. Microstructural observations were performed using both inverted optical microscopy (OM) Leica DMI 5000M and scanning electron microscopy (SEM) JEOL JSM-6490LV. Prior to light microscopy, the specimens were etched by Kroll's reagent (3% HF, 6% HNO_3, 91% distilled water) to unveil the microstructural features. For SEM investigations, a mirror-like OPS polished surface was used. SEM microstructure observations and texture analysis of the joints were conducted using secondary electrons images and electron backscatter diffraction (EBSD). The EBSD measurements were performed for a specimen area of 135 μm × 135 μm at an acceleration voltage of 30 kV, a spot size of 4.7 nA, an emission current of 75 μA, a working distance of 13 mm, a step size of 0.3 μm and a sample tilt angle of 70°. For the orientation calculation, the generalized spherical harmonic series expansion (GSHE) method was applied based on triclinic sample symmetry. The average grain size was measured using the OIM software and the results of EBSD measurements. EDX spectroscopy was used for the local chemical composition determination. For EDX analysis, SEM was operated at an acceleration voltage of 15 kV, a working distance 10 mm and a live time 150 s. The data obtained were calculated based on the standard ZAF method of correction.

2.5. Microhardness testing

Transverse cross sections of the samples for microhardness testing were prepared in the same manner as discussed for the microstructural evaluations. The Vickers microindentation hardness test was carried out using a Zwick/ZHU0,2/Z2,5 universal hardness testing machine and testXpert software. The samples were tested with a 500-g load applied for 15 s according to ASTM E384-11 [10]. The indentation spacing was 200 μm to provide the minimum recommended distance between test points [10]. This resulted in 61 indentations for each line. To investigate thickness gradients, microhardness profiles were measured at three testing positions: radiation exposure side (RES), middle of the weld (M) and the weld root side (RS) (illustrated in **Figure 9**). The distances from RES and RS lines to the edges of the specimen were 200 μm each.

2.6. Residual stress analysis

The distribution of residual stresses in the vicinity of the welding seam was measured by the hole drilling method (HDM) combined with electronic speckle pattern interferometry (ESPI) using a PRISM system, American Stress Technologies Inc. The procedure for residual stress measurement using the HDM is described in ASTM E837 standard [11]. More details about the PRISM system and the theoretical aspects can be found elsewhere [12–14].

All measurements were performed using a high-speed air turbine at rotational speeds of 30,000 rpm, 0.04 mm/s feed rate, using a two-fluted end mill of 0.6 mm diameter. The incremental HDM technique, which involves drilling in a series of small steps in depth, was used in the present work. The holes were drilled to a 0.3 mm depth in 10 steps of 0.03 mm. The geometry of welded plates for HDM measurements and locations of the drilled holes are presented schematically in **Figure 1**. The distance between neighbouring points was provided to be at least 3 mm in accordance with ASTM E-837. The distribution of residual stresses across the welding region, that is, along the *Y* axis in **Figure 1**, was measured by drilling the holes at a number of distances from the weld centreline. At least three points represent each distance in the *Y* direction.

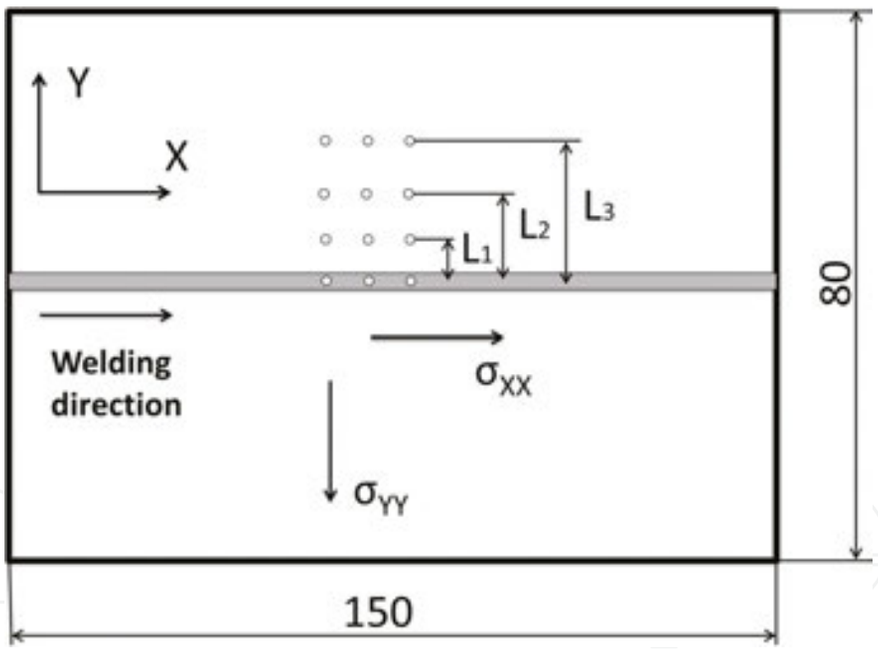

Figure 1. Geometry of welded plates and locations of drilled holes for residual stress measurements.

2.7. Fatigue testing

Load-controlled uniaxial fatigue tests were conducted at room temperature using a Testronic 100 kN RUMUL resonant testing machine. The tests were carried out in accordance with ASTM E466-07 [15] at a frequency of approximately 80 Hz and a stress ratio of $R = 0.1$. The specimen geometry with a uniform test section was chosen for fatigue testing of the LBW Ti-6Al-4V butt

http://dx.doi.org/10.5772/66178

joints in the present work. For all specimens, the welding seam was located in the centre of the gage length, and fatigue loading was applied transverse to the weld direction. The test section in the middle of the S-N specimen had a length of 20 mm (the gage length) and a width of 8 mm. Fatigue properties of the LBW Ti-6Al-4V butt joints were characterized in three conditions: as-welded, machined and heat treated + machined condition. Milling of the surfaces was conducted to remove geometrical defects after welding, such as underfills and reinforcements. The improvement of surface quality after machining was observed. The mean roughness depth, as measured using a contact profilometer in the as-received plate, was 3 μm Rz; after milling, it was 1.5 μm Rz.

For reference, base material fatigue tests were also conducted in the present study. S–N curves were obtained for the base material with the as-received surface quality and after milling. These data must be considered as well, because after machining the weldments flush with the plate surface to remove geometric imperfections, their surface quality is changed significantly, and we cannot further compare the results of the tests with the as-received base material condition. The milled base material should be considered as the reference for machined butt joints. Otherwise, the effect of removing underfills will be overestimated owing to the better quality of the specimen surface after milling. The fatigue limit was determined experimentally as the maximum stress, below which the specimen would not fracture after 10^7 cycles.

2.8. Microfractography

After fatigue testing, the ruptured specimens were selected for further fracture surface examinations. Microfractography is a useful method for understanding the relationship between fracture behaviour and microstructural characteristics. Important clues on the underlying causes of fatigue fracture may be revealed by microfractographical analysis at appropriate magnification. Fracture surfaces of the fatigue specimens were examined using OM and SEM. The SEM observations were performed in secondary electron contrast with 25 kV acceleration voltage and a working distance of 15 mm using the same machine as for metallographic analysis.

3. Results

3.1. Macroscopic appearance of the LBW Ti-6Al-4V butt joints

Visual inspection of laser weldments showed bright silver metallic surfaces from the top and root sides, indicating stable Ar shielding gas atmosphere during the LBW process. All obtained welds were fully penetrated and showed an hourglass shape. A typical transverse cross section of the obtained laser beam welded joint is shown in **Figure 2**. Three distinct regions of the weld are visible: the fusion zone (FZ), heat-affected zone HAZ and base metal (BM). The FZ was distinguished by its columnar dendrites, which grew in the direction from the fusion line to the weld centre (see **Figure 2**). It should be noted that no significant differences between the as-welded and heat-treated conditions regarding the weld geometry were found.

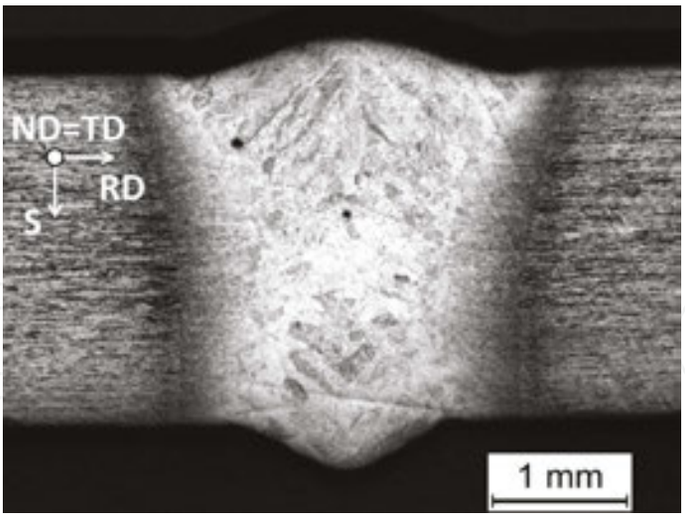

Figure 2. Transverse cross section macrograph of the laser beam welded Ti-6Al-4V butt joint.

The most frequently observed defects in laser weldments of titanium alloys are underfills and porosity [3, 5, 16, 17]. These imperfections are particularly undesirable for structures subjected to cyclic loading because they lead to stress concentration and consequently premature crack formation. The evaporation and expulsion of the molten material from the weld pool and liquid metal flow around the keyhole are dominant processes affecting the formation of underfills [2, 18], which are always present in cases of autogenous laser welding. The use of an additional filler wire in the present work allowed overfilling to be produced and geometrical weld imperfections such as underfills to be partially eliminated. However, filler wire resulted in weld reinforcements from both face and root sides. Abrupt change in the thickness due to weld reinforcement leads to stress concentration at the weld toes and roots and consequently reduces the fatigue strength of the joints. Although the macrograph presented in **Figure 2** reveals almost no underfills, a single weld cross section cannot guarantee the uniformity of the weld profile over the whole length of the seam. This problem can usually be solved by extracting more than one specimen for metallurgical examination. In the present work, the maximum measured underfill depth was approximately 70 μm, which is less than 3% of the specimen thickness. The maximum observed reinforcement was approximately 350 μm. The geometric profile imperfections of laser weldments used in the aerospace industry are strictly limited by several standards: AWS D17.1 [19] and EN 4678 [20]. In terms of underfills and weld reinforcements, EN 4678 is more stringent; the maximum allowed underfill depth for butt joints is 5% of the total thickness and maximum reinforcement is 490 μm for the specimens of the 2.6-mm-thick material. All welds in our work confidently passed the acceptance criteria in terms of the weld profile imperfections for the aerospace industry.

The spherical shape of most pores observed in the present study indicates gas-type porosity. A number of researchers have investigated the main causes of porosity when laser welding titanium alloys [18, 21, 22]. Potential sources for porosity formation are mainly from the presence of excessive hydrogen in the FZ, which is rejected upon solidification, and keyhole instability leading to the entrapment of shielding gases. The investigation of the influence of

http://dx.doi.org/10.5772/66178

welding parameters on the amount of porosity in the laser beam welded Ti-6Al-4V butt joints can be found elsewhere [2, 3, 5].

3.2. Microstructure and microtexture

3.2.1. Base material

The as-received BM microstructure of the 2.6-mm-thick Ti-6Al-4V sheet consists of globular α grains with average grain size of 3.1 ± 0.8 μm and an intergranular retained β, as shown in **Figure 3**. This corresponds to what is known as a mill-annealed microstructure for a hot worked plate that is not fully recrystallized [1]. **Figure 3(a)** shows incompletely recrystallized regions with lamellar morphology, which are not fully transformed to equiaxed α grains upon mill annealing after a hot rolling process. The bright regions in **Figure 3(a)** are the equiaxed or lamellar α grains, and the dark regions are the intergranular β grains distributed at α grain boundaries. Texture analysis is represented by pole figures and inverse pole figures in the cross-sectional plane. It should be kept in mind that the normal to the cross section coincides with the transverse direction of the sheet, and the S direction stands for the thickness direction (see **Figure 2**). The colour in the crystal orientation map (**Figure 3(b)**) is based on a colour-coded inverse pole figure, in which different colours represent different crystallographic orientations. Large red regions in the orientation map correspond to not fully recrystallized lamellar regions. They have the same colour owing to their near-equal crystallographic orientation and were not considered for the calculation of the average grain size.

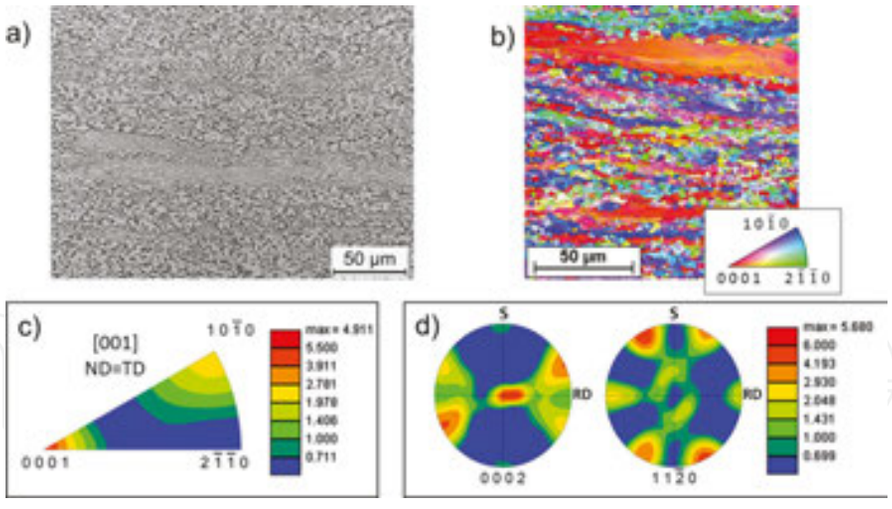

Figure 3. Microstructure of the BM in the as-received condition. (a) OM image, (b) orientation map in the cross section, (c) inverse pole figure, and (d) (0 0 0 1) and (1 1 –2 0) pole figures in the cross-sectional plane.

The base material is characterized by preferred crystal directions such as <0 0 0 1>//ND and <1 0 -1 0>//ND, as shown by the inverse pole figure in **Figure 3(c)**. The microtexture components have been determined using the orientation distribution function (ODF) at sections of $\phi_2 = 0°$ and $\phi_2 = 30°$, where ϕ_2 is an Euler angle. The results analysis showed that the Ti-6Al-4V base material contained the components (0 0 0 1)[2 -1 -1 0] ($f = 12.7$ mrd (multiple of a random

distribution), (0 1 -1 0)[2 -1 -1 4] (4.3 mrd < f < 9.4 mrd) and (0 1 -1 0)[2 -1 -1 0] (f = 1.6 mrd). The (0 0 0 1) pole figure shows that basal planes are aligned in both the rolling direction (RD) and transverse direction (TD) (see **Figure 3(d)**). According to the investigation of Salem [23], this type of texture indicates that the Ti-6Al-4V sheet was cross-rolled. The pole density of the (0 0 0 1) pole figure at RD shows an opening angle of 90° and corresponds to orientation bands at ($\phi_2 = 0°$, $\phi_1 = 60°$ and $\phi_1 = 120°$, $0° \leq \phi \leq 180°$) and ($\phi_2 = 30°$, $\phi_1 = 90°$, $0° \leq \phi \leq 180°$).

3.2.2. Fusion zone

The microstructure of the FZ is characterized by columnar prior β grains that grow from the HAZ in the direction opposite that of the heat flow and impinge at the weld centreline after solidification (see **Figures 2** and **4**). The FZ prior β grain size depends primarily on the weld energy input, with a higher energy input promoting a larger grain size [2, 18, 24]. In the present study, the average prior β grain size in the as-welded condition was approximately 200–300 μm. Within the prior β grains, the FZ predominantly consists of an acicular α' martensitic structure, resulting from the diffusionless $\beta \rightarrow \alpha'$ transformation upon high cooling rates encountered in the LBW process. Ahmed et al. [25] investigated the effect of different cooling rates on microstructural reactions in Ti-6Al-4V and found out that fully α' martensitic transformations take place at cooling rates above 410°C/s. The martensitic microstructure was characterized by long orthogonally oriented thin plates having acicular morphology. **Figure 4(a)** and **(b)** show a similar microstructure in the FZ of laser beam welded Ti-6Al-4V butt joints. Ahmed et al. observed preferential grain boundary formation of secondary α morphology at cooling rates in the range between 410 and 20°C/s. Because no secondary α at prior β grain boundaries was observed in the current work, according to the results of Ahmed et al., we can conclude that the cooling rate in the welding zone was high enough to provide $\beta \rightarrow \alpha'$ diffusionless transformation during LBW. The observed microstructure is typical for fusion zones of laser beam welded [2, 5] and electron beam welded [7, 8] joints.

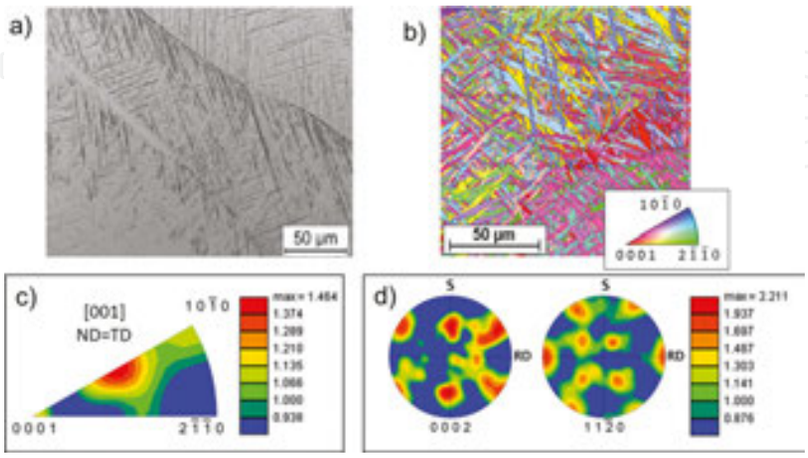

Figure 4. Microstructure of the FZ. (a) OM image of the microstructure, (b) orientation map in the cross section, (c) inverse pole figure, and (d) (0 0 0 1) and (1 1 –2 0) pole figures in the cross section plane.

http://dx.doi.org/10.5772/66178

Local melting and subsequent solidification of Ti-6Al-4V has changed the initial microtexture significantly. The main microtexture components in the FZ are (0 6 -6 1)[8 -3 -5 12] (f = 3.7 mrd), (0 6 -6 1)[-14 5 9 24] (f = 2.2 mrd), (0 1 -1 1)[-4 -1 5 6] (f = 3.3 mrd), (0 2 2 -3)[2 -1 -1 0] (f = 3.2 mrd) and (0 1 -1 1)[2 -1 -1 0] (f = 2.8 mrd), which were examined at 100× magnification to obtain higher statistical weight. The (0 0 0 1)[2 -1 -1 0] component (f = 2.5 mrd) is comparatively much less pronounced (**Figure 4(c)** and **(d)**) than it was in the BM (**Figure 3(d)**). The preferred direction of crystal growth was the <1 1 -2 0>//RD crystal direction during solidification. Furthermore, the presence of <1 1 -2 0>//RD fibre texture is visible.

3.2.3. Heat affected zone

HAZ displays the transition region between the acicular morphology in the FZ and globular structure in the BM. It is usually divided into two subregions based on the β transus temperature. In the HAZ adjacent to the FZ (near-HAZ), the temperatures exceed the β transus during LBW. Consequently, this region consists mostly of the transformed acicular microstructure. Because the temperatures in the HAZ adjacent to the BM (far-HAZ) were lower than the β transus, its microstructure is very similar to that of the BM. Microstructure analysis of both the near-HAZ and far-HAZ is shown in **Figure 5**.

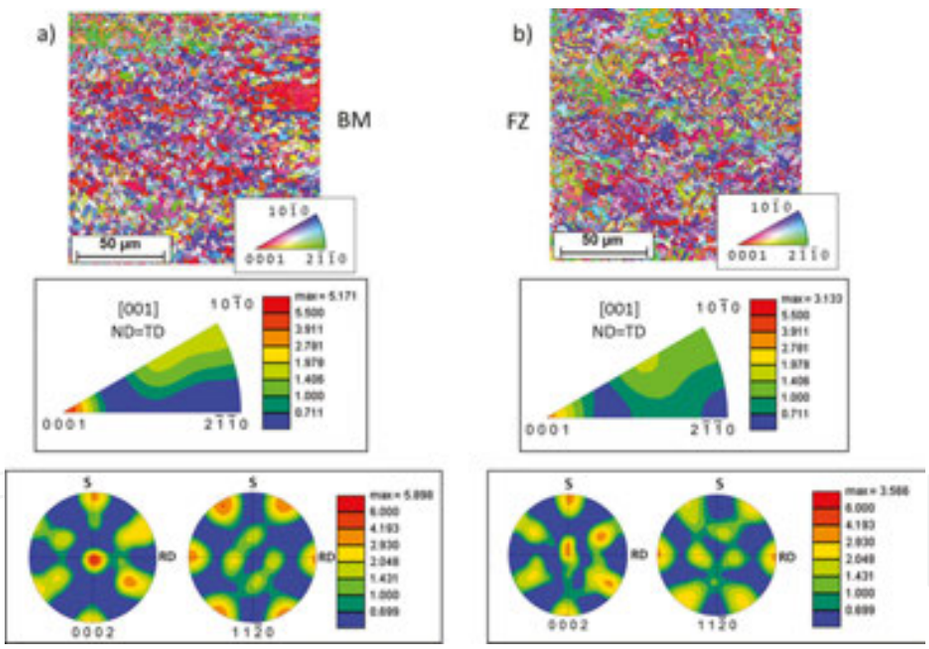

Figure 5. Microstructure of the HAZ in the as-welded condition. Orientation maps, inverse pole figures and pole figures of the HAZ adjacent to the BM (a) and the HAZ adjacent to the FZ (b).

The microstructure of the HAZ zone adjacent to the BM (1.4 mm from the weld centre) remained nearly the same after thermal cycles were imposed by the LBW process but was characterized by finer globular grains having an average grain size of 2.1 ± 0.7 μm and wider distribution of crystal directions between <0 0 0 1>//ND and <1 0 -1 0>//ND compared with that of the base material (**Figure 5(a)**). The main component is still (0 0 0 1)[2 -1 -1 0]] (12.1 mrd <

f < 12.8 mrd); however, (0 1 -1 0)[2 -1 -1 0] was superimposed by (0 8 -8 1)[2 -1 -1 0] (f = 6.5 mrd), leading to misorientations between 3.6° and 4.4°. The BM component (0 1 -1 0)[2 -1 -1 4] has been dissolved, and new components such as (0 6 -6 5)[5 -5 0 6] (f = 6.4 mrd) and (0 3 -3 -4)[14 3 -17 15] (f = 9.4 mrd) have emerged within the orientation band (ϕ_2 = 0°, ϕ_1 = 60°, 0° < ϕ < 80°). The misorientations of these components are 26.2° and 37.3° with regard to (0 1 -1 0)[2 -1 -1 4]. The orientation band (ϕ_2 = 0°, ϕ_1 = 120°, 0° < ϕ < 180°) showed the occurrence of further components such as (0 5 -5 1)[-3 1 2 5] (f = 5.6 mrd) and (0 6 -6 5)[-8 9 -1 12] (f = 4.6 mrd), resulting in misorientations of 7.7° and 24.7° with regard to (0 1 -1 0)[-2 1 1 4] (see pole figure in **Figure 5(a)**). The misorientations between the base material and heat-affected zone indicate microstructural distortion of the laser beam welded Ti-6Al-4V butt joint due to heat input and subsequent rapid cooling during the joining process.

A significant change in microstructure was observed for the near-HAZ at a distance of 1.05 mm from the FZ (**Figure 5(b)**). The equiaxed initial microstructure of the base material was transformed into an acicular morphology with a small amount of embedded globular grains. The transformation was connected with a grain refinement and a weakening of the (0 0 0 1)[2 -1 -1 0] component dominating the BM and HAZ adjacent to the BM. Some of the crystals rotated around the angles between 4.6° and 4.8°, which led to formation of (0 0 0 1)[4 -7 3 0] (5.9 mrd < f < 6.5 mrd). A further portion of crystals rotated around the <2 -1 -1 0>//RD crystal direction and tilted at an angle of 10.3°, resulting in the formation of the (0 1 -1 -1)[2 -1 -1 0] component (f = 7.3 mrd). Furthermore, the microstructure transformation led to the formation of new components such as (0 3 -3 2)[14 -12 -2 15] (f = 4.5 mrd), (0 1 -1 -1)[1 0 -1 1] (f = 2.1 mrd), (0 1 -1 -1)[-6 -1 7 8] (f = 3.9 mrd) and (0 1 -1 -1)[-17 19 -2 21] (f = 3.0 mrd) and to dissolution of (0 6 -6 5)[5 -5 0 6]. The (1 1 -2 0) pole figure shows a tendency towards the formation of <1 1 -2 0>//RD fibre texture present in the FZ also (**Figure 4(d)**).

3.2.4. Influence of heat treatment on the microstructure

EBSD analysis of heat-treated specimens revealed no significant texture transformations upon PWHT. The main texture components remained approximately the same with slight deviations in numerical values of peaks. Thus, our further attention will be focused mainly on the microstructural characteristics, which can be clearly seen from the OM observations. **Figure 6** shows the influence of PWHT on the average grain size in the BM. Heat treatments at temperatures less than 750°C did not change the grain size in the BM significantly (**Figure 7(a)**, **(b)**). Recrystallization processes leading to coarsening of the microstructure were activated at higher temperatures starting from 800°C (FA2, DA). The maximum average grain size was achieved after DA and was 4.9 ± 1.5 μm. OM images of the BM microstructure after PWHT at temperatures higher than 750°C are shown in **Figure 7**. From this figure, it can be seen that α phase is fully recrystallized after duplex annealing, and almost all lamellar regions were transformed into equiaxed grains (**Figure 7(c)**). All other conditions of PWHT that are not shown in **Figure 7** led to almost the same microstructure as in the starting condition, and these images are omitted.

http://dx.doi.org/10.5772/66178

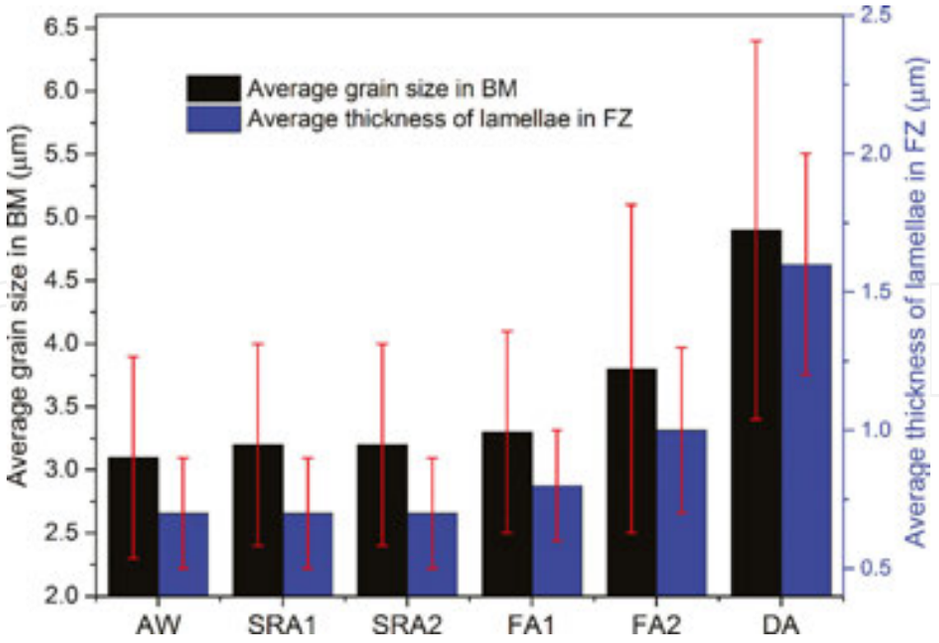

Figure 6. Influence of PWHT on the average grain size in the BM and the width of lamellae in the FZ.

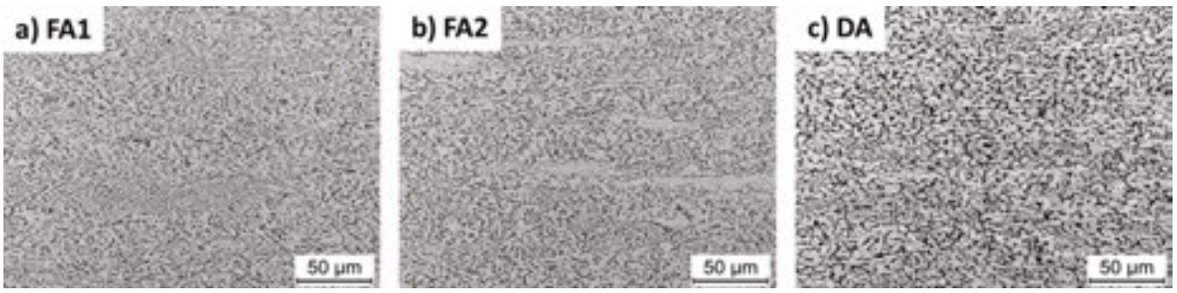

Figure 7. Influence of PWHT on the microstructure of the BM.

Light microscopic investigations yielded that heat treatments up to 650°C (SRA2) did not affect the microstructure of the FZ significantly because such low temperatures were insufficient for martensite decomposition into equilibrium $\alpha + \beta$ structure. Sallica-Leva et al. [26] studied the effects of heat treatment on the mechanical properties of an acicular α' martensite obtained by selective laser melting. In their work, the microstructure of samples heat treated at 650°C was very similar to that of the starting condition, whereas significant grain coarsening was observed after heat treatment at 800°C. The precipitation of β phase and the gradual transformation of α' into α phase by the diffusion of excess vanadium from α' to β phase were proposed to be the main events of martensite decomposition. Their results are in a good agreement with our findings. **Figure 6** shows the influence of PWHT on the average thickness of α' (α) laths in the FZ. Significant grain coarsening of the microstructure was observed after PWHT at temperatures higher than 750°C. This result is a consequence of the transformation of fine martensitic morphology into an equilibrium lamellar $\alpha + \beta$ structure and diffusion-controlled growth of

obtained platelets at high temperatures (**Figure 8**). Starting from 750°C (FA1), a secondary α phase at prior β grain boundaries designated as grain boundary α [25] starts to appear (**Figure 8(b)** and **(c)**). Furthermore, the thickness of grain boundary α gradually increases with increasing PWHT temperature. After DA, the colonies of parallel α plates are formed upon recrystallization processes. In the case of the martensitic structure, fine α' needles are nearly orthogonal, and α colonies are not so pronounced (see **Figure 4(b)**). As we can see in **Figure 8(c)**, in DA condition, the α colony size is clearly visible and is approximately 20–30 μm. These α colonies should not be confused with prior β grains. The prior β grain size was not altered after PWHT; it was an order of magnitude larger than the α colony size and cannot be seen in **Figure 8**.

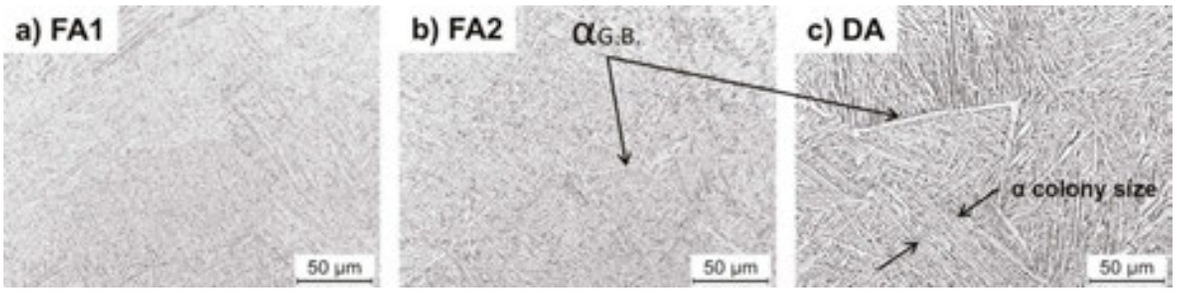

Figure 8. Influence of PWHT on the microstructure of the FZ.

Because the HAZ has a bimodal microstructure and consists of equiaxed primary α grains in transformed β matrix, the effect of PWHT on the HAZ microstructure is somehow the combination of the above-mentioned effects on the BM and FZ, that is, coarsening of primary α grains and transformation of fine martensitic structure into coarse lamellar.

3.3. Microhardness

The distribution of microhardness across the laser beam welded Ti-6AL-4V butt joint in the as-welded condition is presented in **Figure 9**. No significant difference in microhardness profiles among three testing positions was found; that is, no thickness gradient was observed in the present study. The average microhardness value of the base material was found to be 336 ± 8 HV 0.5. The FZ exhibited the highest average microhardness, approximately 396 ± 10 HV 0.5 (roughly 18% greater than that in the BM), and it decreased abruptly as the distance from the FZ line increased. The microhardness distribution within the FZ was quite uniform without significant deviations from the average value. This result is related to the use of Ti Grade 5 as a filler wire material. In the case of LBW with Ti Grade 2 (commercially pure Ti) filler material, a significant decrease in microhardness in the centre of the FZ was observed [27].

The increase in microhardness from the BM via the heat-affected zone to the FZ centre is correlated with local changes in microstructure, which were activated during LBW and subsequent cooling. The occurrence of maximum hardness in the FZ is related to the formation of a strong martensitic structure due to high cooling rates upon solidification. Acicular α' phase produced by the diffusionless transformation from the high-temperature β phase field exhibits

http://dx.doi.org/10.5772/66178

higher strength and lower ductility, which are attributable to the fine size of martensitic plates and high defect density [28]. The influence of microtexture plays a minor role because <0 0 0 1>//ND and <1 0 -1 0>//ND crystal directions were aligned parallel to the indentation direction in both the BM and HAZ despite decreasing axial intensity. HAZ is characterized by strong inhomogeneity and plays a role of a transition zone from acicular martensitic morphology within the FZ to equiaxed microstructure in the BM. The strong spatial variation of the microstructure, namely, the decrease in the martensitic content, leads to a high gradient of microhardness inside the HAZ. Squilace et al. [2] reported that the hardness gradient in the HAZ is inversely proportional to the heat input during LBW.

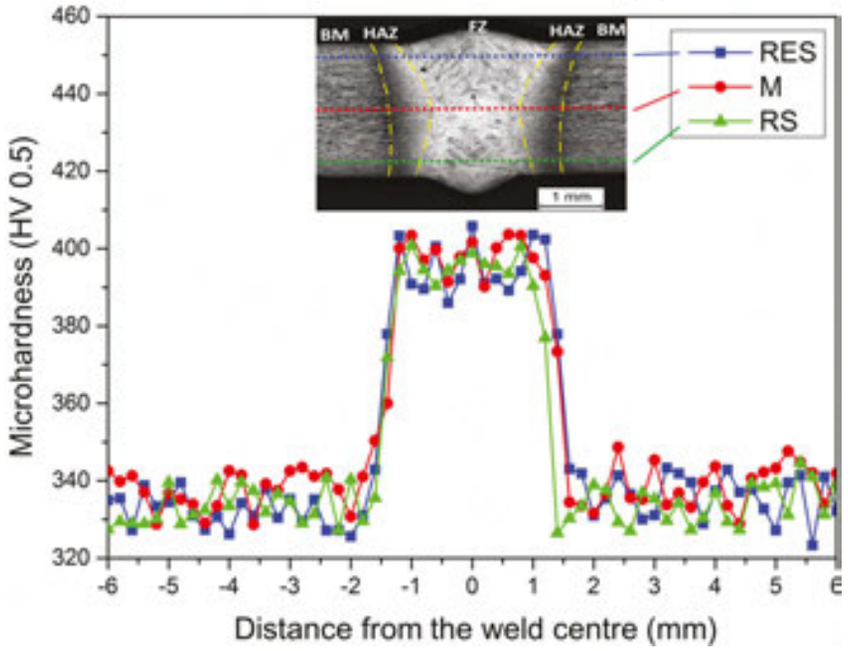

Figure 9. Microhardness profile of the laser beam welded Ti-6Al-4V butt joint measured in the as-welded condition.

3.3.1. Influence of PWHT on microhardness

The variations of average microhardness values for the BM and FZ in the as-welded condition and after PWHT under different conditions are shown in **Figure 10**. The hardness in the FZ was generally higher than that in the BM, but their difference depended strongly on the annealing temperature. The changes in microhardness after conducting PWHT are strictly related to the microstructural changes that occurred during the PWHT. Because the effect of PWHT depends on the initial microstructure, the BM and FZ underwent different transformations during PWHT and will be discussed separately.

Annealing at 540°C for 4 h slightly increased the average microhardness of the BM from 336 ± 8 HV 0.5 in the as-welded condition to 351 ± 10 HV 0.5 after annealing. This unexpected hardening effect upon low-temperature annealing was not evident from OM and SEM observations and can be attributed to precipitation hardening of the α phase by coherent Ti_3Al

particles [1, 28]. During annealing, significant alloy element partitioning takes place; that is, α phase is enriched with α stabilizing elements (Al), and β phase is enriched with β stabilizing elements (V, Fe) owing to diffusion processes. This fact was proved by EDX point analysis. **Figure 11** shows the average content of alloying elements in α and β phases of the BM after PWHT. As shown in **Figure 11**, Al content in the α phase and V and Fe content in the β phase increase with increasing temperature. Coherent α_2 particles can then be precipitated in the alpha phase by ageing owing to increased Al content. This age-hardening effect of the α phase in Ti-6Al-4V by Ti_3Al particles was well documented by Lutjering et al. [28]. In the Ti-6Al-4V alloy, the Ti_3Al solvus temperature is approximately 550°C. Annealing at temperatures lower than 550°C will precipitate α_2 particles, whereas a heat treatment at 600°C will be only a stress-relieving treatment [29]. The latter was in a good agreement with our findings. Heat treatment at 650°C for 1 h led to average microhardness in the BM of 331 ± 10 HV 0.5, which is slightly lower than that in the starting condition. Evidence of this ageing phenomenon is not apparent from optical microscopy images and EBSD results because the size of the α_2 particles is approximately several nanometres as reported in Ref. [28]. The application of transmission electron microscopy (TEM) techniques to study this complex phenomenon should improve identification of the α_2 phase.

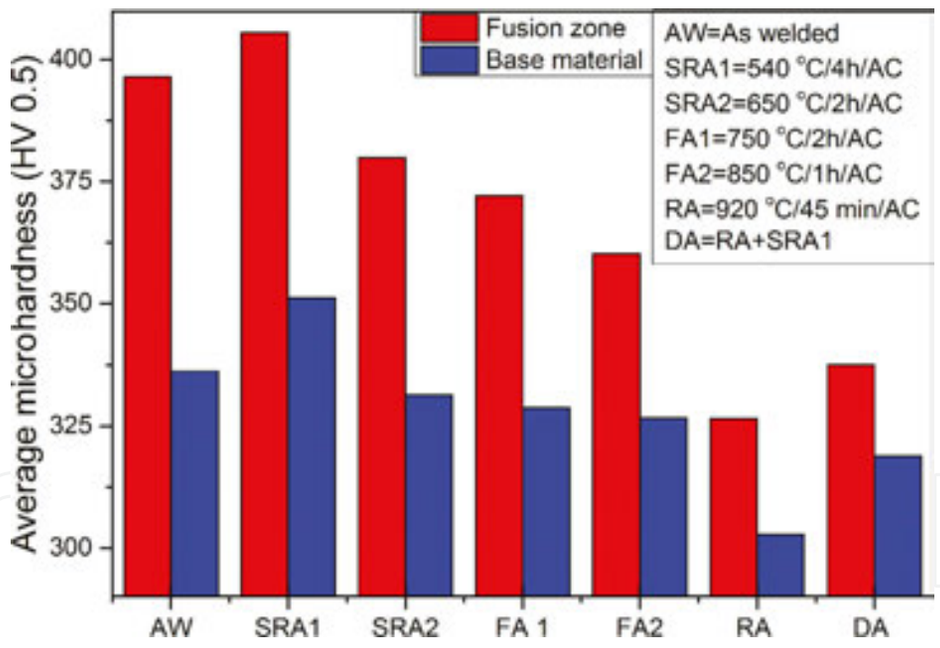

Figure 10. PWHT influence on the average microhardness in the FZ and BM.

As presented in **Figure 10**, annealing in the temperature range of 650–850°C does not affect the average microhardness in the BM significantly, and It gradually decreased with increasing temperature. A substantial decrease in microhardness was observed after recrystallization annealing at 920°C for 45 min. These results are related to grain coarsening in accordance with the Hall-Petch mechanism and are consistent with microstructural observations discussed in the previous section. Because the second step of duplex annealing is equal to SRA1 heat

http://dx.doi.org/10.5772/66178

treatment, this led to hardening of the coarsened structure obtained after RA due to precipitation of α_2 phase as discussed above.

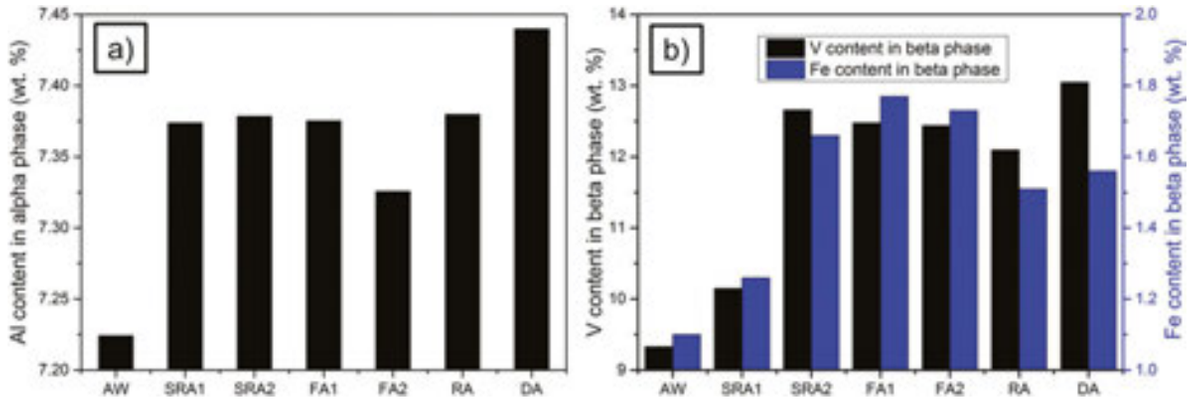

Figure 11. Alloying element partitioning in the BM due to PWHT. (a) Al in α phase and (b) V and Fe in β phase.

The effect of various PWHT on the average microhardness in the FZ has a generally very similar trend as discussed for the BM; however, the mechanisms leading to these results were not the same because the initial microstructures were completely different. The hardening effect observed in the FZ after SRA1 annealing can be attributed to tempering of the martensitic structure. This effect at relatively low temperatures has already been observed by a number of researchers [6, 30, 31]. Because metastable α' martensite is supersaturated in β stabilizers owing to the diffusionless transformation $\beta \rightarrow \alpha'$, upon annealing, it decomposes into $\alpha + \beta$ by precipitation of incoherent β particles at dislocations or β phase layers at plate boundaries [28]. Chesnutt et al. [32] investigated ageing of β-quenched Ti-6Al-4V and used TEM to show microprecipitation of β phase particles in tempered martensite. Precipitation hardening takes place only after SRA1 annealing, whereas heat treatment at 650°C for 2 h leads to partial decomposition of martensite with attendant reduction of microhardness. Starting from the temperature of 750°C, grain coarsening of an acicular microstructure in the FZ is responsible for the gradual reduction of microhardness with increasing temperature (see **Figure 10**). After recrystallization, the annealing microstructure in the FZ was completely transformed into equilibrium coarse lamellar $\alpha + \beta$ morphology with the lowest hardness values nearly equal to that of the BM in the as-received condition. The hardening mechanism that took place after ageing in DA was apparently the same as described above for the BM because after recrystallization, both the BM and FZ consisted of equilibrium $\alpha + \beta$ phases.

3.4. Residual stress analysis

The HDM method gives the average stresses in the area where the material was drilled, that is, in the circle of 0.6 mm in diameter. Because no depth-dependent gradient of residual stresses was observed in the present study, each point is represented by the mean value of residual stresses at the depth of 0.3 mm. The distribution of residual stresses longitudinal and transverse to the weld line across the welding seam is shown in **Figure 12(a)**. High tensile longitudinal

stresses up to 650 MPa are produced in the weld itself and the immediately adjacent parent material during solidification. These high tensile residual stresses near the weld are balanced by compressive longitudinal stresses further from the weld line. Transverse residual stresses have a similar profile but are an order of magnitude lower than the longitudinal component with a maximum value not exceeding 50 MPa. Our results are in good agreement with that reported by Cao et al. for laser beam welded Ti-6Al-4V alloy [33].

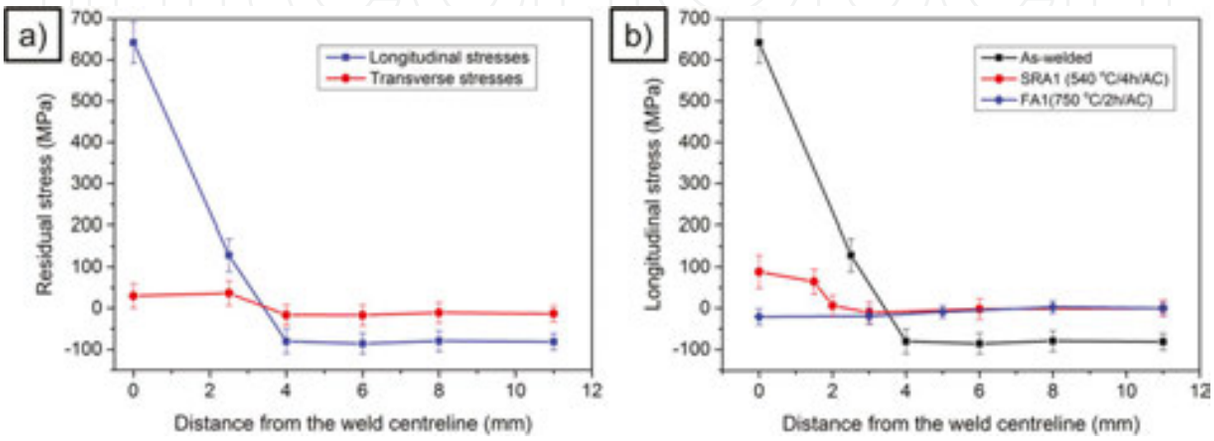

Figure 12. Residual stress distribution in the vicinity of the laser beam welded Ti-6Al-4V butt joint. (a) Residual stresses in the as-welded condition and (b) influence of PWHT on longitudinal residual stress profile.

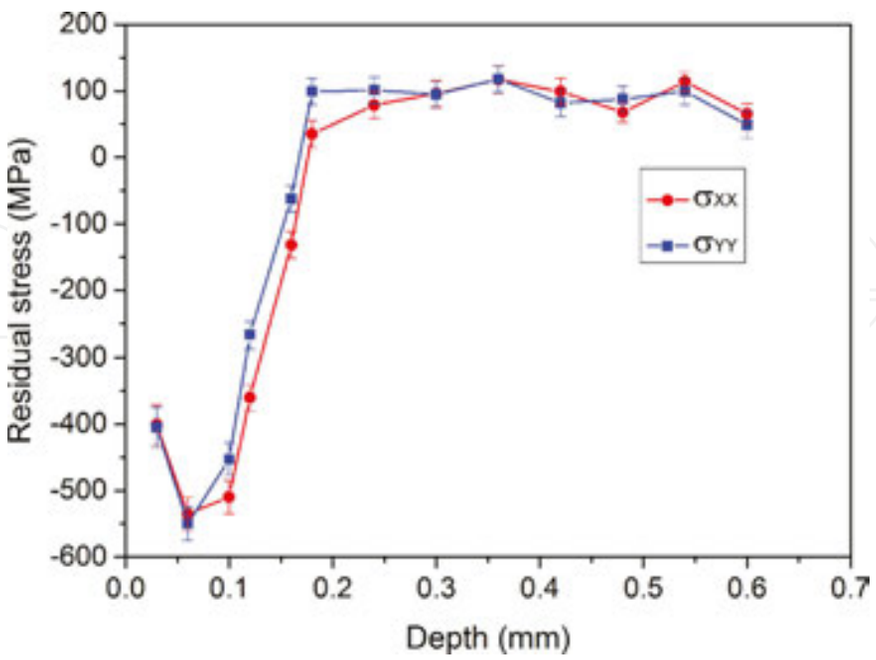

Figure 13. Residual stresses in the BM after milling.

http://dx.doi.org/10.5772/66178

The stress-relieving effect at elevated temperatures due to PWHT is presented in **Figure 12(b)**. Because longitudinal stresses significantly prevail over transverse components, for simplicity, **Figure 12(b)** presents only the evolution of longitudinal stresses upon heat treatment. Annealing at 540°C results in the stress relief from 650 MPa in the centre of FZ to approximately 90 MPa (nearly 85% effect). After heat treatment at 750°C, almost full stress relief was achieved, and PWHT's at higher temperatures completely remove welding-induced residual stresses in the welding seam. It should be kept in mind that the presented results correspond to different specimen geometry from that used in fatigue testing. The specimen size should be considered as an influential factor when evaluating the effect of residual stresses on the fatigue of welded joints [34, 35]. After extracting S–N specimens from the welded plate due to the relatively short width of the gauge length (8 mm), residual stresses are almost fully removed. The latter was confirmed by the HDM technique in the extracted fatigue specimens and does not allow us to make any conclusions about the influence of residual stresses on the fatigue properties of laser beam welded Ti-6Al-4V butt joints. However, in the situations in which the width of the tested specimen is sufficient to keep the residual stresses after cutting or the welding line is parallel to the external stresses, the results presented in this work would be quite useful. Moreover, the stress-relieving effect investigated here is necessary for comprehensive analysis of the PWHT of laser beam welded butt joints. Large-scale specimens must be tested to separately investigate the influence of residual stresses on the fatigue of LBW joints.

Incremental HDM allowed us to investigate the residual stresses that arise in the surface layer after machining. These stresses are of great interest because they significantly affect the unnotched fatigue properties of the material and will be discussed in the last section. **Figure 13** shows a residual stress distribution in the BM after milling. As we can see, high compressive residual stresses up to 550 MPa are formed in the 0.2-mm-thick surface layer. These compressive stresses in the surface layer are balanced by tensile stresses in the bulk material.

3.5. Fatigue testing

The results of room-temperature high cycle fatigue tests are shown in **Figures 14** and **16**. For reference, base material data are also provided in **Figure 14**. Arrows indicate non-failures after 10^7 cycles (run-outs). The curves shown in these plots represent the mean lines corresponding to 50% probability of survival. The results highlight the inherent scatter in fatigue test experiments for titanium alloys [36]. As shown in **Figure 14**, the fatigue limit of the BM in the starting as-received condition is approximately 650 MPa or nearly 65% of the yield strength. Machining both reduces the surface roughness from 3 to 1.5 Rz and results in the formation of compressive residual stresses in the 0.2-mm-thick surface layer (see **Figure 13**). Improved surface quality and introduction of favourable compressive stresses in the near surface region have a beneficial effect on the HCF resistance of the Ti-6Al-4V BM. As seen in **Figure 14**, the fatigue limit increased to 720 MPa after milling the surface of the specimens. This result should be kept in mind when comparing the effect of milling the weld defects on the HCF properties. The S-N curve of the milled BM must be considered as the reference for machined weldments.

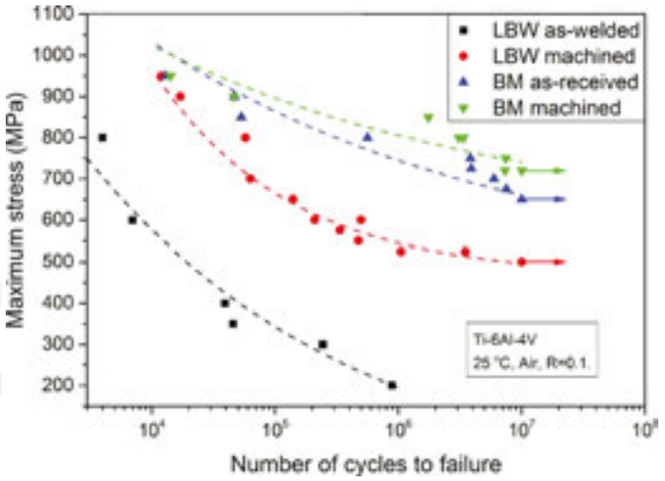

Figure 14. Influence of machining on the fatigue behaviour of the laser beam welded Ti-6Al-4V butt joints.

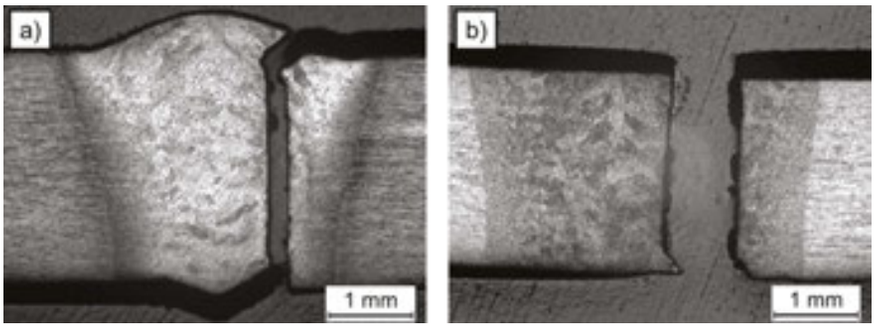

Figure 15. Transverse cross sections of fractured S-N specimens. (a) As-welded condition, 200 MPa, 889,500 cycles and (b) annealed (FA2) and machined, 575 MPa, 4,953,100 cycles.

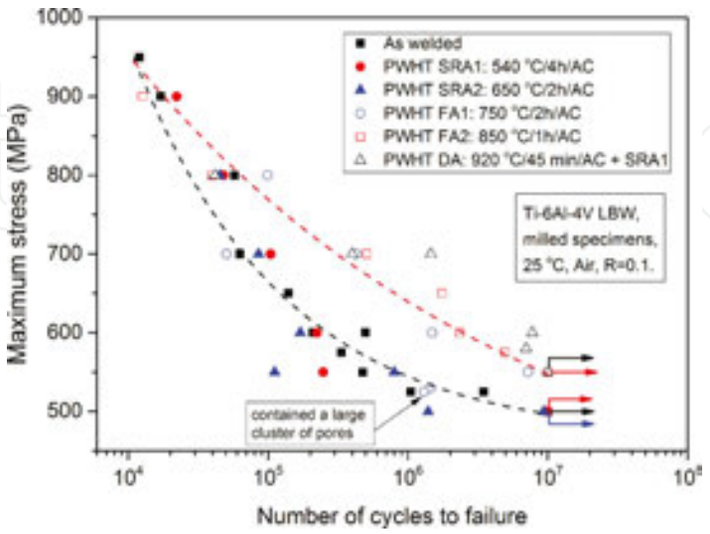

Figure 16. Influence of PWHT on the fatigue behaviour of the laser beam welded Ti-6Al-4V butt joints.

http://dx.doi.org/10.5772/66178

3.5.1. Influence of defects

The S-N curves for the as-welded and machined flush laser beam welded Ti-6Al-4V butt joints are given in **Figure 14**. The fatigue limit after milling the weldment flush with the sheet surface was approximately 500 MPa. This value corresponds to 70% of the base material fatigue limit (also machined). It can be seen (**Figure 14**) that the presence of reinforcements and small underfills significantly deteriorates the fatigue of the laser beam welded butt joints. Geometry imperfections such as underfills and reinforcements play the role of stress concentrators (notches). The failure always occurred in the welding seam initiated at the face or root underfill. **Figure 15** shows typical transverse cross sections of fractured S-N specimens in the as-welded and machined conditions. In the as-welded specimen, the crack started from the weld root and propagated through the FZ perpendicular to the direction of applied stress as shown in **Figure 15(a)**.

Thus, machining the weld reinforcements and underfills flush with the sheet surface can be considered as an easy method to improve the fatigue performance of the laser beam welded butt joints. These results are consistent with the work of Squillace et al. [2]. They showed that the fatigue strength of autogenous laser beam welded Ti-6Al-4V butt joints is strongly influenced by the value of the underfill radius, and the S-N curves shift towards the region of HCF as the value of the underfill radius increases. Improved fatigue strength by partially or totally eliminating the underfills, predicted in the above-mentioned work, was confirmed in the present study. The use of filler wire partly prevented the formation of underfills; however, as seen in **Figure 14**, the synergetic effect of the weld reinforcements and underfills considerably affected the fatigue performance, although the acceptance criteria in terms of geometrical defects were passed.

In the low cycle fatigue (LCF) region, the S-N curve of the milled condition approaches the static strength of the laser beam welded joints, which usually equals the strength of the parent material [2, 5]. The specimen tested at the 950 MPa level of maximum stress was fractured in the base metal. This implies that in the LCF region, the laser beam welded Ti-6Al-4V flush milled butt joints exhibit a BM level of fatigue strength. All other laser beam welded specimens tested in the current work were fractured in the FZ. The typical location of failure in the machined laser beam welded joint is shown in **Figure 15(b)** for the specimen, which endured nearly five million cycles at the 575 MPa level of maximum stress.

In the HCF regime, the S-N curve for the flush milled condition is located lower than that of the base material. The fatigue limit decreased by nearly 31%. This result implies the existence of internal microstructural features or defects deteriorating the fatigue strength of the joint. In experiments with butt welds in the as-welded condition, the stress concentration at the weld toes or roots is much more severe than that due to minor defects existing in the welding zone, and these defects are therefore less important. Thus, geometry features can overshadow the microstructural effects and internal defects. The latter are of primary interest in this work. By removing the stress concentrators from the surface of the welding seam, internal defects become the most important notches in the joint and exhibit their full deleterious effect.

3.5.2. Influence of PWHT on fatigue

The influence of PWHT on the fatigue performance of the laser beam welded Ti-6Al-4V butt joints is shown in **Figure 16**. It should be kept in mind that all data given in **Figure 16** represent the flush milled condition. If the annealing temperature is lower than 750°C, the results of the tests lie in the scattering range of the as-welded S-N curve. No significant influence of low-temperature annealing ($T < 750$°C) on fatigue performance was found. Conditions SRA1 and SRA2 had approximately the same fatigue limit of approximately 500 MPa, considering the inherent scatter of fatigue experiments.

Annealing at temperatures above 750°C leads to the slight improvement of fatigue properties. The specimens annealed at 850°C (FA2) and subjected to DA showed the highest value of fatigue limit in the present work: 550 MPa. For comparison, as-welded specimens heat treated at lower temperatures endured less than 500,000 cycles at that level of stress. The fatigue limit for the FA1 condition was not achieved in the current study. The last two FA1 specimens exhibited very low fatigue life compared with the position of other points for this condition. The examination of fracture surfaces revealed the presence of relatively large clusters of pores with the size of approximately 300 μm. These specimens were probably extracted from the region of the plate with worse quality of the welding (run-in or run-outs). Even considering the scatter of the results, the general trend, that annealing at high temperatures (>750°C) increases the fatigue strength of the joint and shifts the S-N curve towards higher values of stresses, can be clearly seen in **Figure 16**.

3.6. Microfractography

Fracture surfaces were studied using OM and SEM to identify the locations of crack initiation, region of stable crack propagation and overload region morphology. After careful fracture surface examination of the broken S-N specimens with an optical microscope, it was concluded that almost 100% of these failures started from internal welding defects, that is, pores with average diameters of approximately 10–100 μm. These pores play the role of structural discontinuities and stress concentrators (notches). The existence of such high stresses in the specimen leads to the initiation of the microcracks in very early periods of fatigue life [37]. **Figure 17** shows the fracture surface overall views of the heat-untreated machined specimen (a) and the specimen after PWHT at 850°C for 1 h (b). Crack initiation sites are clearly seen. The typical distance from the surface to the crack nucleation point is approximately 300–700 μm; however, less frequently, pores appear closer to the surface. Cracks initiated from a single pore are very rare and occur only if the size of the pore is approximately 100 μm. More frequently, the cracks start from the subsurface clusters of pores (usually two or three pores), as shown in **Figure 17(a)**. The distance between cracks in subsurface clusters is typically less than the pore diameter and does not exceed 10 μm. According to AWS D17.1 [19], two or more discontinuities in the welding zone should be treated as one when the spacing between them is less than the dimension of the larger discontinuity. This allows us to consider subsurface clusters of pores as single defects with an approximate size of 150–250 μm.

The area around the crack initiation site is slightly brighter than the region of stable crack growth. This white circle resembles a "fish eye" fracture, common for steels in the ultra-long-

http://dx.doi.org/10.5772/66178

life regime, when fatigue fracture origins are mostly at non-metallic inclusions in the subsurface [37]. The "fish eye" in the present study always had a radius equal to the distance from the surface to the crack nucleation site. The difference in the colours is probably caused by cyclic contact of the fracture surfaces in the absence of atmospheric effects within the "fish eye" and by cyclic contact of the fracture surfaces in the presence of atmospheric gases outside the "fish eye" [37].

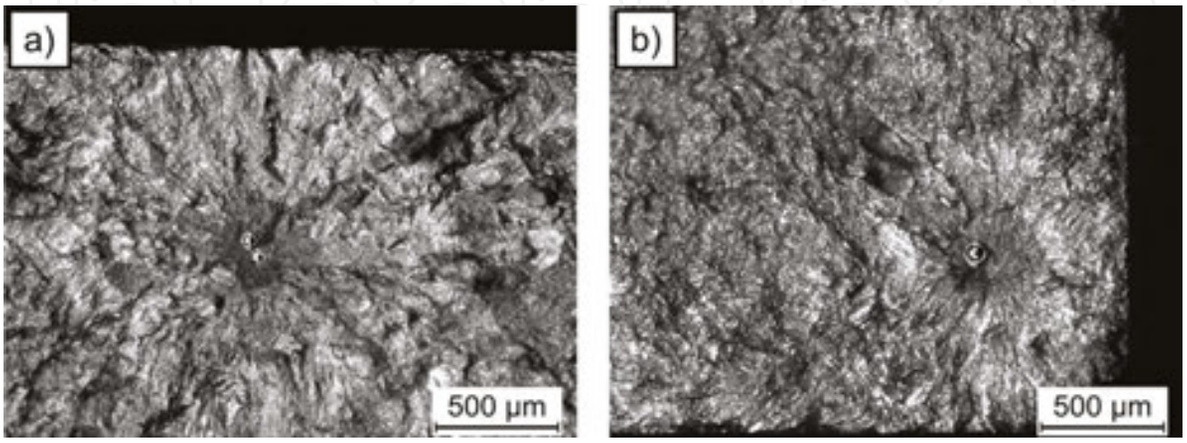

Figure 17. OM images of fracture surfaces. (a) As-welded condition, 525 MPa, 3,488,300 cycles and (b) PWHT (FA2), 650 MPa, 1,763,300 cycles.

The SEM images with higher magnification of the specimen shown in **Figure 17(b)** revealing the topography of the fracture surface in different zones of crack growth are shown in **Figure 18**. The zone adjacent to the pore (**Figure 18(a)**) is characterized by low values of stress intensity factor and shows fibrous morphology. A comparison of the fracture face with the microstructure (see **Figure 8**) suggests that the elongated fracture features correspond to individual α laths. The crack propagated radially from the pore and was dominated by a transgranular mode of cracking. At high stress intensity factors (**Figure 18(b)**), the fracture topography was mainly characterized by typical fatigue striations and secondary cracks. The overload region exhibited small, shallow dimples, which are indicative of ductile fracture due to microvoid coalescence (**Figure 18(c)**).

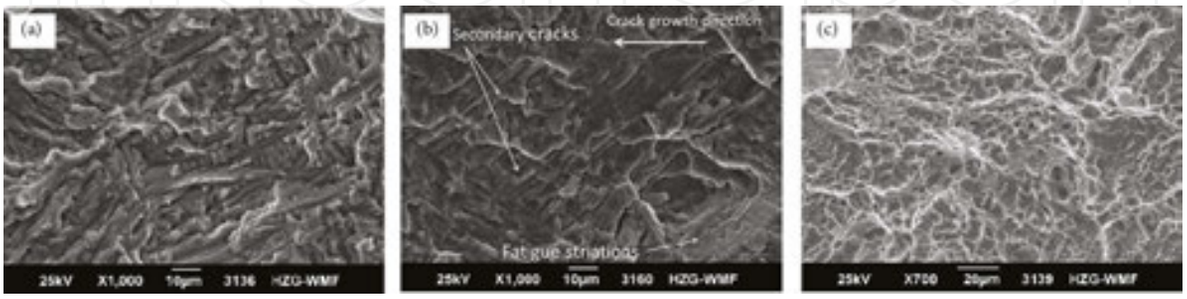

Figure 18. SEM images of fatigue fracture surfaces. PWHT (FA2), 650 MPa, 1,763,300 cycles. (a) Region close to the pore, (b) region of stable crack growth, and (c) overload region, final fracture.

4. Discussion

Because the specimens that were subjected to PWHT were milled thereafter, we can assume that equality of surface roughness was provided, and we can exclude this factor from our further consideration. This allows us to consider microstructural changes as the main factor affecting the fatigue properties of the laser beam welded joints in the present work. The aim of this section is to link the results of mechanical testing with microstructural observations, microhardness measurements and fracture surface topography analysis. As described above, fatigue failure in the laser beam welded joints was always found in the FZ. Thus, the microstructure in this region of the weldment is a crucial factor affecting the fatigue performance of the joints.

The HCF failure process comprises four stages: microcrack initiation, microcrack propagation, macrocrack propagation and final fracture [38]. The border between micro- and macrocrack propagation can be defined when the size of the crack is approximately one order of magnitude larger than the effective microstructural size [39], which is the average grain size (3–6 μm) in the case of an equiaxed microstructure and is the α colony size (10–40 μm, depending on the cooling rate) in the case of a lamellar structure. A number of researchers have shown that crack initiation and microcrack propagation take up to 95% of the high cycle fatigue life [28, 37, 40]. Macrocrack propagation is very fast relative to the first stages and does not play any significant role in unnotched HCF. In the presence of defects, the size and sharpness of notches are of great importance because they determine the size of the plastic zone at the tip of the notch. As already mentioned above, we can consider subsurface clusters of pores as single defects with approximate sizes of 150–250 μm. A sharp notch with a small crack at its tip may be regarded as a crack [37]. Because the transition short/long crack is on the order of 200 μm (10 times the microstructural size) for lamellar microstructures, a crack emanating from the pore in the FZ can already be assumed to be a long one after the initiation period. This brings us to an important conclusion that the HCF of the LBW joints primarily depends on crack initiation from the pore and near-threshold macrocrack propagation.

A comprehensive study on the influence of microstructural variables on near-threshold fatigue behaviour of macrocracks in titanium Ti-6Al-4V was conducted by Yoder et al. [41–43]. Bilinear crack growth rate behaviour was observed, with two distinct branches that independently obey the power law and join together in the transition point (ΔK_T). In the region $\Delta K_{th} < \Delta K < \Delta K_T$ (ΔK_{th} stands for the threshold stress intensity factor), the cyclic plastic zone is less than the effective grain size, and a microstructurally sensitive mode of crack growth occurs that involves crystallographic bifurcation in grains adjacent to the crack plane. In contrast, in the region $\Delta K > \Delta K_T$, the grains within a larger plastic zone deform as a continuum, which results in a microstructurally insensitive, non-bifurcated mode of crack growth. The observed values of ΔK_T were in remarkable agreement with predictions according to the equation $\Delta K_T = 5.5\ \sigma_y\ v d$, where σ_y is the yield strength of material, and d is the effective microstructural size. In the case of titanium alloys, the Hall–Petch relation is relatively weak [44], so the d term in the above-mentioned equation dominates, leading to the increase of ΔK_T with increasing grain size. The inverse dependence of fatigue crack growth rates upon grain size was directly related to the

http://dx.doi.org/10.5772/66178

microstructurally sensitive mode of crack growth because larger bifurcated cracks occur with increasing grain size.

The most influential microstructural parameter on the mechanical properties of lamellar (platelet) microstructures is the α colony size (packet size) because it determines the effective slip length in lamellar structures [28, 41]. This parameter should be considered as the effective microstructural size for lamellar morphology in the FZ. With increasing α colony size, the unnotched fatigue strength and yield stress decrease because smooth HCF strength depends primarily on the resistance to crack nucleation and microcrack propagation. However, if macrocracks or sharp notches already exist in the material, a coarse lamellar microstructure is more beneficial for fatigue performance because increased effective slip length retards fatigue crack propagation due to increased crack front roughness. The trade-off between decreased strength and increased fracture toughness makes the coarse lamellar microstructure less sensitive to notches and more advantageous for usage in applications, in which notched fatigue performance is the crucial factor.

Annealing of the laser beam welded Ti-6Al-4V butt joints at temperatures up to 650°C is insufficient for full martensite decomposition into an equilibrium lamellar $\alpha + \beta$ structure in the FZ and recrystallization in the BM. The width of individual α lamellae and the average α colony size remained almost the same after heat treatments at low temperatures. Hence, mechanical properties also should have remained approximately the same. We can conclude that the low-temperature annealing does not affect the HCF performance of the laser beam welded Ti-6Al-4V butt joints.

As described above, starting from the temperature of 750°C, the metastable martensitic structure in the FZ transforms to equilibrium platelet $\alpha + \beta$ morphology, as shown in **Figure 8**. With increasing temperature during PWHT, the width of individual lamellae and α colony size increases with a commensurate increase in the effective slip length and a corresponding decrease in the yield stress. A coarse lamellar structure with lower density of defects after annealing at high temperatures has lower strength and higher ductility than martensitic morphology [6, 45, 46]. This was indirectly confirmed by the decreased microhardness in the FZ after PWHT at high temperatures. Although the static strength of the joint decreased slightly, more ductile and softer material in the FZ was more beneficial for the HCF of laser beam welded joints than a hard martensitic structure. High-temperature annealing reduced the notch sensitivity of the FZ, and internal defects were less detrimental for fatigue properties than in a martensitic structure. Increased α colony size and consequently larger effective slip length leads to a more bifurcated crack growth profile and increased crack propagation resistance of the material. This result is consistent with the works of Yoder et al. [41–43] and Lütjering and Williams [28].

To verify our assumptions, transverse cross sections of fractured specimens were made. Grinding and polishing was performed to the plane containing the pore to compare the crack front roughness in different conditions. As shown in **Figure 19**, the coarser lamellar microstructure displayed a more tortuous and deflected crack path than the finer-scale martensitic microstructure in the region adjacent to the pore, where the crack growth is sensitive to the microstructure. The effective slip length in the case of annealed material is the α colony size,

but in case of martensitic morphology, it is the width of individual α plates. Increased crack path tortuosity leads to enhanced crack deflection and a resulting increase in the FCP resistance and the overall fatigue performance.

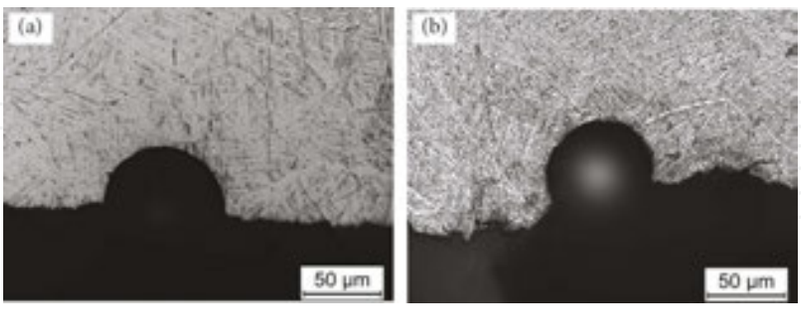

Figure 19. Comparison of crack front roughness profiles in the zone adjacent to the pore. (a) As welded condition and (b) annealed at 850°C for 1 h.

The effect of grain size on the notch sensitivity is well known for steels. Murakami [37] investigated microcrack propagation starting from artificial holes with diameters of 35–500 μm in steels. They concluded that defects smaller than a critical size are non-damaging (not detrimental) to fatigue strength, and the critical size is smaller for materials having higher static strength. Harder material is more sensitive to notches and defects. A larger decrease in fatigue strength for materials of higher static strength was found. This trend is generally in reasonable agreement with our findings, although we investigated different materials. Based on the results for steels, we can also assume the existence of non-damaging permissible defects for titanium alloys because micromechanisms and models for the behaviour of cracks emanating from sharp notches do not depend on the material. However, further investigations must be carried out to prove this assumption. If the dependence of critical size on the microstructure of the FZ is obtained, an obvious way to exclude the detrimental effect of pores on fatigue is to provide a welding technique leading to smaller pores than the critical size. However, it should be kept in mind that in the absence of pores or if the size of defects is lower than the critical size, PWHT will have an opposite effect on fatigue; that is, fatigue strength will be reduced after high-temperature annealing. This was shown in the work of Babu et al. [7] for electron beam welded joints. The fatigue cracks in their work originated at the surface, implying that internal defects were insignificant. PWHT at temperatures of approximately 900°C reduced the fatigue strength of the joints at $2 \cdot \times 10^6$ cycles compared to that of the as-welded condition and those annealed at lower temperatures.

5. Conclusions

Fully penetrated Ti-6Al-4V butt joints were produced by LBW with filler wire. The effect of PWHT was analysed in terms of microstructural features, microhardness, residual stress distribution and fatigue performance. The following conclusions can be drawn:

http://dx.doi.org/10.5772/66178

1. The microstructure of the laser beam welded seam in the as-welded condition was characterized by strong inhomogeneity due to high cooling rates imposed by the welding process. FZ consists of a metastable martensitic structure formed by the diffusionless $\beta \rightarrow \alpha'$ transformation. High spatial gradients of the microstructure and microtexture in the HAZ result in mechanical properties mismatch between the BM and FZ, which was indirectly confirmed by the microhardness profile.

2. Significant grain coarsening was found after PWHT at temperatures higher than 750°C owing to recrystallization processes in the BM and martensite decomposition in the FZ. After high-temperature annealing, the BM microstructure has much fewer lamellar regions, and in the FZ, α at prior β grain boundaries appears, and pronounced α colonies are formed.

3. In the as-welded condition, microhardness values in the FZ were 18% higher than those in the BM. Annealing at 540°C led to the hardening of both the FZ owing to the tempering of martensite and the BM owing to precipitation of α_2 phase. Annealing in the temperature range of 650–920°C promotes grain coarsening in the BM and martensite decomposition in the FZ. As a result, microhardness decreased with increasing temperature. Duplex annealing allowed the microhardness mismatch between the FZ and BM to be minimized to 6%.

4. Annealing at 540°C for 4 h had an effect of relieving approximately 85% of stress. PWHT at higher temperatures completely eliminated welding residual stresses. Machining of the weld defects produces compressive residual stresses in the 0.2-mm-thick surface layer, which are beneficial for fatigue.

5. The fatigue limit of a laser beam welded machined butt joint was 500 MPa or 70% of the milled BM fatigue limit. Stress concentration due to underfills and reinforcements significantly deteriorates the fatigue performance. PWHT at temperatures higher than 750°C increase the fatigue limit by approximately 10% up to 550 MPa. The failures of machined samples started from the subsurface clusters of pores. Increased crack front roughness in the microstructure-sensitive region of crack propagation and increased critical size of non-damaging defects are supposed to be the most influential factors leading to improved fatigue properties of laser beam welded Ti-6Al-4V butt joints subjected to PWHT. A slight decrease in static strength is the main offset for this method.

Author details

Fedor Fomin*, Volker Ventzke, Falk Dorn, Nikita Levichev and Nikolai Kashaev

*Address all correspondence to: fedor.fomin@hzg.de

Institute of Materials Research, Materials Mechanics, Helmholtz-Zentrum Geesthacht, Geesthacht, Germany

References

[1] Boyer R, Welsch G, Collings EW, editors. Materials Properties Handbook: Titanium Alloys. 1st ed. Materials Park, OH: ASM International; 1994. pp. 483–633.

[2] Squillace A, Prisco U, Ciliberto S, Astarita A. Effect of welding parameters on morphology and mechanical properties of Ti-6Al-4V laser beam welded butt joints. Journal of Materials Processing Technology. 2012;212(2):427–436. DOI: 10.1016/j.jmatprotec.2011.10.005

[3] Kabir ASH, Cao X, Medraj M, Wanjara P, Cuddy J, Birur A. Effect of welding speed and defocusing distance on the quality of laser welded Ti-6Al-4V. In: Materials Science and Technology; October 17–21, 2010; Houston, Texas; 2010. pp. 2787–2797.

[4] Ahn J, Chen L, Davies CM, Dear JP. Parametric optimisation and microstructural analysis on high power Yb-fibre laser welding of Ti–6Al–4V. Optics and Lasers in Engineering. 2016;86:156–171. DOI: 10.1016/j.optlaseng.2016.06.002

[5] Kashaev N, Ventzke V, Fomichev V, Fomin F, Riekehr S. Effect of Nd:YAG laser beam welding on weld morphology and mechanical properties of Ti–6Al–4V butt joints and T-joints. Optics and Lasers in Engineering. 2016;86:172–180. DOI: 10.1016/j.optlaseng.2016.06.004

[6] Kabir ASH, Cao X, Gholipour J, Wanjara P, Cuddy J, Birur A, Medraj M. Effect of postweld heat treatment on microstructure, hardness, and tensile properties of laser-welded Ti-6Al-4V. Metallurgical and Materials Transactions A. 2012;43(11):4171–4184. DOI: 10.1007/s11661-012-1230-5

[7] Babu NK, Raman SGS, Srinivasa Murthy CV, Reddy GM. Effect of beam oscillation on fatigue life of Ti-6Al-4V electron beam weldments. Materials Science and Engineering A. 2007;471:113–119. DOI: 10.1016/j.msea.2007.03.040

[8] Tsai CJ, Wang LM. Improved mechanical properties of Ti–6Al–4V alloy by electron beam welding process plus annealing treatments and its microstructural evolution. Materials and Design. 2014;60:587–598. DOI: 10.1016/j.matdes.2014.04.037

[9] Edwards P, Ramulu M. Fatigue performance of friction stir welded Ti–6Al–4V subjected to various postweld heat treatment temperatures. International Journal of Fatigue. 2015;75:19–27. DOI: 10.1016/j.ijfatigue.2015.01.012

[10] ASTM E384-11, Standard Test Method for Knoop and Vickers Hardness Of Materials, ASTM International, West Conshohocken, PA, 2011. DOI: 10.1520/E0384-11E01.

[11] ASTM E837-13a, Standard Test Method for Determining Residual Stresses by the Hole-Drilling Strain-Gage Method, ASTM International, West Conshohocken, PA, 2013. DOI: 10.1520/E0837.

[12] Steinzig M, Ponslet E. Residual stress measurement using the hole drilling method and laser speckle interferometry, Part I. Experimental Techniques. 2003;27(3):43–46.

[13] Schajer G, Steinzig M. Full-field calculation of hole-drilling residual stresses from ESPI data. Experimental Mechanics. 2005;45(6):526–532. DOI: 10.1007/BF02427906

[14] Schajer GS, Prime MB. Use of inverse solutions for residual stress measurements. Journal of Engineering Materials and Technology. 2006;128(3):375–382.

[15] ASTM E 466-15, Standard Practice for Conducting Force Controlled Constant Amplitude Axial Fatigue Tests of Metallic Materials, ASTM International, West Conshohocken, PA, 2015. DOI: 10.1520/E0466-15

[16] Blackburn JE, Allen CM, Hilton PA, Li L, Hoque MI, Khan AH. Modulated Nd:YAG laser welding of Ti–6Al–4V. Science and Technology of Welding and Joining. 2010;15(5): 433–439. DOI: 10.1179/136217110X12731414739718

[17] Blackburn J, Allen CM, Khan A, Hilton PA, Li L. Dual focus Nd:YAG laser welding of titanium alloys: effect on porosity formation. Lasers in Engineering. 2012;22(5–6):319–336.

[18] Cao X, Kabir ASH, Wanjara P, Gholipour J, Birur A, Cuddy J, Medraj M. Global and local mechanical properties of autogenously laser welded Ti-6Al-4V. Metallurgical and Materials Transactions A. 2014;45:1258–1272. DOI: 10.1007/s11661-013-2106-z

[19] AWS: Specification for Fusion Welding for Aerospace Application, D17.1, Miami, OH: American Welding Society; 2001.

[20] DIN EN 4678:2012-01. Aerospace series – Weldments and brazements for aerospace structures – Joints of metallic materials by laser beam welding – Quality of Weldments, European Committee for Standardization, Brussels, 2011.

[21] Chaturvedi MC, editor. Welding and Joining of Aerospace Materials. Woodhead Publishing Ltd; 2012. pp. 94–102

[22] Blackburn J, Allen C, Hilton P, Li L. Nd:YAG laser welding of titanium alloys using a directed gas jet. Journal of Laser Applications. 2010;22(2):71–78.

[23] Ayman A. Salem. Texture separation for a/b titanium alloys. In: Schwartz A.J, Kumar M, Adams B.L, Field D.P, editors. Electron Backscatter Diffraction in Materials Science. 2nd ed. Springer; 2009; pp. 317–327. DOI: 10.1007/978-0-378-88136-2

[24] Peters M, Williams JC. Microstructure and Mechanical properties of a welded (α+β) Ti Alloy. Metallurgical Transactions A. 1984;15:1589–1596.

[25] Ahmed T, Rack HJ. Phase transformations during cooling in α+β titanium alloys. Materials Science and Engineering A. 1998;243(1–2):206–211. DOI: 10.1016/S0921-5093(97)00802-2

[26] Sallica-Leva E, Caram R, Jardini AL, Fogagnolo JB. Ductility improvement due to martensite a' decomposition in porous Ti-6Al-4V parts produced by selective laser

melting for orthopedic implants. Journal of the Mechanical Behavior of Biomedical Materials. 2016;54:149–158. DOI: 10.1016/j.jmbbm.2015.09.020

[27] Kashaev N, Ventzke V, Horstmann M, Riekehr S, Yashin G, Stutz L, Beck W. Microstructure and mechanical properties of laser beam welded joints between fine-grained and standard Ti-6Al-4V sheets subjected to superplastic forming. Advanced Engineering Materials. 2015;17(3):374–382. DOI: 10.1002/adem.201400202

[28] Lütjering G, Williams JC. Titanium. 1st ed. Berlin, Heidelberg: Springer-Verlag; 2003.

[29] Lutjering G. Influence of processing on microstructure and mechanical properties of (α+β) titanium alloys. Materials Science and Engineering A. 1998;243(1–2):32-45.

[30] Thomas G, Ramachandra V, Ganeshan R, Vasudevan R. Effect of pre- and post-weld heat treatments on the mechanical properties of electron beam welded Ti-6Al-4V alloy. Journal of Materials Science. 1993;28:4892–4899.

[31] Wang SQ, Liu JH, Chen DL. Effect of post-weld heat treatment on the fatigue properties of dissimilar titanium alloy joints. In: 13th International Conference on Fracture; June 16–21, 2013; Beijing, China. DOI: 10.4028/www.scientific.net/AMR.891–892.1539

[32] Chesnutt JC, Rhodes CG, Williams JC. Relationship between mechanical properties, microstructure, and fracture topography in α+β titanium alloys. In: 78th Annual Meeting of the ASTM. The Symposium on Fractography – Microscopic Cracking Processes, ASTM STP 600, American Society for Testing and Materials. 1976, 99–138.

[33] Cao Z, Che Z, Zou S. The residual stress distribution and fatigue property of TC4 laser-welded joint treated by laser shock peening. In: 5th International Conference on Information Engineering for Mechanics and Materials; January 2015; Atlantis Press; pp. 631–635. DOI: 10.2991/icimm-15.2015.119

[34] Masubuchi K. Analysis of Welded Structures. Oxford/New York: Pergamon Press; 1980.

[35] Gurney TR. Fatigue of Welded Structures. 2nd ed. Cambridge: Cambridge University Press; 1979. 456 p.

[36] Schijve J. Fatigue of Structures and Materials. 2nd ed. Springer; 2009. pp. 373–394.

[37] Murakami Y. Metal Fatigue: Effects of Small Defects and Nonmetallic Inclusions. 1st ed. Oxford: Elsevier; 2002. 369 p.

[38] Anderson TL. Fracture Mechanics: Fundamentals and Applications. 2nd ed. CRC Press LLC; 1995. 688 p.

[39] Suresh S, Ritchie RO. Propagation of short fatigue cracks. International Metals Reviews. 1984;29(6):445–475.

[40] Eylon D, Pierce CM. Effect of microstructure on notch fatigue properties of Ti-6Al-4V. Metallurgical Transactions A. 1976;7:111–121.

[41] Yoder GR, Cooley LA, Crooker TW. Fatigue crack propagation resistance of beta-annealed Ti-6Al-4V alloys of differing interstitial oxygen contents. Metallurgical Transactions A. 1978;9A:1413–1420.

[42] Yoder GR, Cooley LA, Crooker TW. Quantitative analysis of microstructural effects on fatigue crack growth in Widmanstatten Ti-6Al-4V and Ti-8Al-1Mo-1V. Engineering Fracture Mechanics. 1979;11:805–816.

[43] Yoder GR, Cooley LA, Crooker TW. Observations on microstructure sensitive fatigue crack growth in a Widmanstatten Ti-6Al-4V alloy. Metallurgical Transactions A. 1977;8A:1737–1743.

[44] Yoder GR, Cooley LA, Crooker TW. A critical analysis of grain-size and yield-strength dependence of hear-threshold fatigue crack growth in steels. In: Fracture mechanics: 14th Symposium – Volume I; ASTM STP 791; 1983. p. 361.

[45] Fan Y, Shipway PH, Tansley GD, Xu J. The effect of heat treatment on mechanical properties of pulsed Nd:YAG welded thin Ti-6Al-4V. Advanced Materials Research. 2011;189–193:3672–3677.

[46] Cao X, Jahazi M, Marya S, Birur A. Effect of post-weld heat treatment on Nd:YAG laser welding Ti6Al4V alloy quality. Materials Science Forum. 2010;638–642:3655–3660. DOI: 10.4028/www.scientific.net/MSF.638-642.3655

IntechOpen

IntechOpen

IntechOpen